American Mineralogist, Volume 93, pages 1816–1822, 2008

Timescales of spherulite crystallization in obsidian inferred from water concentration profiles

Jonathan M. Castro,[1,*] Pierre Beck,[2] Hugh Tuffen,[3] Alexander R.L. Nichols,[4] Donald B. Dingwell,[5] and Michael C. Martin[6]

[1]Department of Mineral Sciences, Smithsonian Institution, MRC-119, Washington, D.C. 20013, U.S.A.
[2]Laboratoire de Planetologie de Grenoble, 122 rue de la Piscine, Grenoble 38041, France
[3]Environmental Science Department, Lancaster University, Bailrigg, Lancaster LA1 4YW, U.K.
[4]Institute for Research on Earth Evolution (IFREE), Japan Agency for Marine Earth Science and Technology (JAMSTEC), 2-15 Nasushima-cho, Yokosuka, Kanagawa 237-0061, Japan
[5]Earth and Environmental Sciences, LMU-University of Munich, Theresienstrasse 41/III, 80333 Munich, Germany
[6]Advanced Light Source, Lawrence Berkeley National Laboratory, Berkeley, California 94720, U.S.A.

Abstract

We determined the kinetics of spherulite growth in obsidians from Krafla volcano, Iceland. We measured water concentration profiles around spherulites in obsidian by synchrotron Fourier transform infrared spectroscopy. The distribution of OH^- groups surrounding spherulites decreases exponentially away from the spherulite-glass border, reflecting expulsion of water during crystallization of an anhydrous paragenesis (plagioclase + SiO_2 + clinopyroxene + magnetite). This pattern is controlled by a balance between the growth rate of the spherulites and the diffusivity of hydrous solute in the rhyolitic melt.

We modeled advective and diffusive transport of the water away from the growing spherulites by numerically solving the diffusion equation with a moving boundary. Numerical models fit the natural data best when a small amount of post-growth diffusion is incorporated in the model. Comparisons between models and data constrain the average spherulite growth rates for different temperatures and highlight size-dependent growth among a small population of spherulites.

Keywords: Spherulite, diffusion, obsidian, crystallization

Introduction

The rates and timescales of magmatic processes exert first-order control over the behavior of magmatic systems. For example, the rate of decompression during magma ascent may dictate the manner in which volatiles are released from the melt, ultimately influencing degassing and the explosivity (e.g., Gonnermann and Manga 2007). Similarly, crystallization in volcanic conduits and lava flows may generate excess volatile pressure, leading to nonlinear extrusion and endogenous dome explosions (e.g., Sparks 1997). Clearly, our ability to model magmatic processes depends on accurate determinations of timescales of processes such as crystallization and bubble growth.

Direct measurement of the timing and duration of magmatic phase changes (e.g., crystallization) is challenging due to the extreme inaccessibility of magmatic environments; efforts to do so have been relegated to analyzing natural crystal chronometers in quenched rocks. Crystal-size distribution (CSD) analysis, for example, has provided estimates of crystal growth rates in magmatic systems (e.g., Cashman 1988). However, temporal information based on CSD interpretations may be subject to large errors, owing to the uncertainties of the underlying laws governing crystal growth, including assumptions that the growth rates of all crystals was the same.

Advances in timescale determinations have been made by analyzing chemical gradients within crystals (Costa and Dungan 2005) and glasses (Castro et al. 2005) combined with diffusion modeling of the elemental distributions. Here, we build on these studies by determining the crystallization timescales of small spherical crystal aggregates in obsidian, known as spherulites (Fig. 1). We present synchrotron Fourier transform infrared spectroscopic (SFTIR) measurements of water concentration profiles around spherulites in obsidian. We then model the concentration profiles by numerically solving the advection-diffusion equation for a range of temperatures to yield model crystallization timescales.

Geological background

Spherulites are radiating, commonly concentrically arranged aggregates of one or more anhydrous minerals set in a glassy matrix (Fig. 1). They occur in obsidian domes, large-volume vitrophyric ash-flow tuffs (e.g., Smith et al. 2001), and in shallow volcanic conduits (e.g., Stasiuk et al. 1996).

Spherulites are inferred to have nucleated and grown in response to large undercoolings (>200 °C) rapidly imposed on the magma by its degassing and quenching (e.g., Swanson et al. 1989). As dictated by the thermal profile of the magma body (Manley 1992), spherulitic obsidian develops in spatially restricted zones (e.g., Manley and Fink 1987; Stevenson et al. 1994), comprising a transitional facies that separates the rapidly quenched, outermost vitrophyric rhyolite from a devitrified

* E-mail: castroj@si.edu

microcrystalline core.

Anomalously high volatile contents exist within and just above the spherulitic zones in lava domes (e.g., Westrich et al. 1988). Several authors have suggested a genetic link between spherulite crystallization and the increase in volatile pressure within lava domes (e.g., Wright 1915), although to date there is only circumstantial evidence supporting such a "second boiling" phenomenon (Manley and Fink 1987). Below we present the first direct evidence for water concentration gradients around spherulites. We use this information to quantitatively estimate the kinetics of spherulite growth.

Samples and methods

Decimeter-sized rhyolitic obsidian samples were collected from the Hrafntinnuhryggur ridge system on Krafla volcano, Iceland. These obsidians come from a small (~5 m tall) outcrop that is part of an elongate series of domes marking the roof of a dike that intruded an ice sheet (Tuffen and Castro, in preparation). Doubly polished wafers, 100–200 μm thick were prepared from 5 obsidian samples. The spherulites are numerous, mostly spherical, randomly spaced, and of a limited size (~50–800 μm). As a result, the intersection planes of the wafers commonly expose 1 to 3 spherulites along their maximum (equatorial) dimension. Using this geometry, we have been able to relate the variation in H_2O species to the radial growth direction of the spherulites.

H_2O concentrations were determined by SFTIR at the Advanced Light Source, Lawrence Berkeley National Laboratory. Measurements were made along traverses oriented perpendicular to the spherulite-glass boundaries on a Thermo Nicolet Magna 760 FTIR spectrometer interfaced with a NicPlan IR microscope (at beamline 1.4.3). The IR beam has a diffraction-limited diameter of about 3 μm. The uncertainty in spot position is ±2 μm. Transmittance spectra were obtained over the mid-IR (1400–4000 cm^{-1}) to the near-IR (3700–6500 cm^{-1}) regions with MCT detectors, KBr beam-splitters, and the synchrotron light source. 128 scans were used to obtain each spectrum and these spectra were corrected by subtracting a background spectrum collected every hour. We determined OH^- concentrations from the intensity of the broad 3570 cm^{-1} absorption band, utilizing an absorption coefficient of 100 $L \cdot mol \cdot cm^{-1}$ (Newman et al. 1986). We estimate the analytical uncertainty of OH^- concentration to be ±10% of the measured value.

Spherulite mineralogy was determined by (1) microscopic observation; (2) sample magnetism to identify Fe-oxides as magnetite; and (3) compositional data from energy dispersive spectra (EDS) collected on a field-emission SEM at the Smithsonian Institution National Museum of Natural History, Washington, D.C. The SEM was operated at 10–12 KeV, 1 mm working distance, and beam current ranging from 0.5–1 nanoamps. Precise identification of spherulite minerals was challenging due to the small size (often <2 μm) of individual phases (Fig. 1) and their intimate, interlocking growth habits (Fig. 2), which invariably resulted in the electron beam sampling parts of neighboring phases. However, where possible, we analyzed the largest regions of a continuous phase. Mineralogic determinations were made based on the peaks that appeared in the EDS specta; minor peaks nested within the background radiation were not used to infer mineralogy.

The glass transition temperature of the Krafla obsidian was determined by differential scanning calorimetry using a Netzsch DSC 404C at the University of Munich following the procedure of Gottsmann et al. (2002).

Glass compositions were analyzed using a JEOL JXA-8900R electron microprobe (EPMA) running software with ZAF corrections at the Smithsonian National Museum of Natural History. Analyses were performed with an accelerating voltage of 15 keV, a 10 μm beam, and a 10 nA beam current. Standardization was performed on the following natural mineral standards: quartz (Si), anorthite (Ca), bytownite (Al), microcline (K), albite (Na), hornblende (Fe, Mg). A natural rhyolitic glass (VG568) of known major-element composition was periodically analyzed to check for instrument drift.

Analytical results

Spherulites consist of, in order of modal abundance, sodic plagioclase (~45%), an SiO_2-polymorph, quite possibly quartz (~40%), clinopyroxene (~3%), and magnetite (~1–2%; Fig. 2). In addition, the largest spherulites (>500 μm) contain a small amount (<15 vol%) interstitial glass and microvesicles (<1 vol%). This phase assemblage accounts for most of the major elements analyzed on bulk samples of the Krafla rhyolite (Table 1); however, K appears to have behaved incompatibly during spherulite crystallization as it was not detected in any of the phases. Like water, K is probably concentrated in the surrounding glass matrix.

The plagioclase and the SiO_2-polymorph textures (Figs. 1 and 2) mimic micrographic, micropoikilitic, and granophyric intergrowths observed in nature and produced experimentally (e.g., MacLellan and Trembath 1991). In both cases, the SiO_2-phase often hosts plagioclase microlites.

Spherulites are typically enclosed in haloes of colorless rhyolitic glass (Table 1), which separate them from the pervasive brown matrix glass (Fig. 1). Glass color differences correspond to different oxidation states of Fe (Galliard et al. 2003). In cross-polarized light, the colorless glass regions are birefringent, as evidenced by their first-order gray color (Fig. 1b). Spherulites commonly overprint pyroxene- and Fe-oxide microlite-defined flow banding, however, in one sample, microlites are deflected around the spherulites (Fig. 1c).

Figure 3 shows a subset of OH^- concentration profiles; the complete analytical data are reported in Table 2. The area under the OH^- concentration profiles is proportional to the amount of water surrounding each spherulite that is elevated above the far-field matrix concentration. We quantified this water enrichment by fitting the OH^- concentration profiles with polynomials and then integrating from the point of maximum OH^- content to the far-field matrix value (Table 2). We then subtracted the area corresponding to the background water concentration from the total area under the curve to get the amount of water in excess of the far-field value. Concentrations were converted from wt% to milligram units by multiplying the volume of glass having elevated water by a glass density of 2.326 g/cm^{-1}, determined from the major-element chemistry of the glass (Table 1) using the method of Ghiorso and Sack (1995). The resultant mass of glass was then multiplied by the weight fraction of OH^- measured in the elevated region.

The amount of water surrounding spherulites increases with the spherulite size, and in most cases, matches the amount of water that would be expelled during complete crystallization of anhydrous minerals from a volume of melt equal to the volumes of each spherulite (Table 2), as determined by their radii. Differences between the measured and predicted water show that some spherulites retained water during their growth (e.g., as seen in OR1305_A), consistent with the presence of a small amount of glass and microvesicles in some of them.

Table 1. Representative electron microprobe analyses of obsidian from Obsidian Ridge, Krafla volcano

Major oxide (n = 136)	wt%	(st. dev.)
SiO_2	75.0	0.75
TiO_2	0.22	0.02
Al_2O_3	12.0	0.19
FeO	3.23	0.92
MnO	0.11	0.04
MgO	0.1	0.02
CaO	1.68	0.13
Na_2O	4.19	0.17
K_2O	2.75	0.10
Total	99.3	0.65

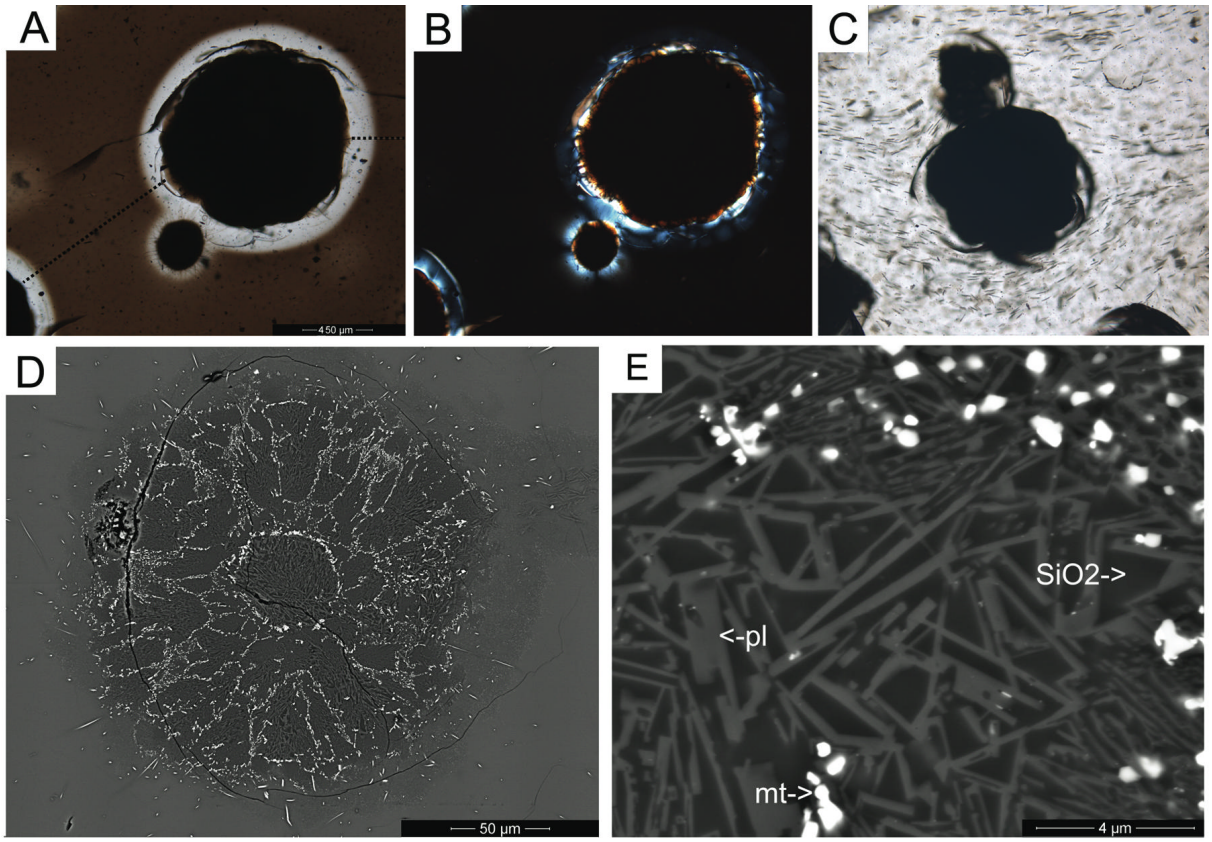

FIGURE 1. Photomicrographs of spherulites in obsidian. (**a**) Spherulites (round, black) viewed in plane-polarized light. Matrix is rhyolitic glass of variable oxidation state, providing the different colors. Two SFTIR measurement traverses are shown for reference (profiles OR1305_SPH1_prf1 and 2a). (**b**) Same spherulite as in **a**, only viewed in cross-polarized light. Bright fringes are due to strain birefringence from hydration. (**c**) Spherulite in glass matrix showing flow-oriented microlites (slender black rods) deflected around the spherulite. Scale is the same as in **a**. (**d**) Back-scattered electron (BSE) images of spherulites. Interiors consist mostly of plagioclase (pl), an SiO_2-polymorph (SiO_2), and magnetite (mt).

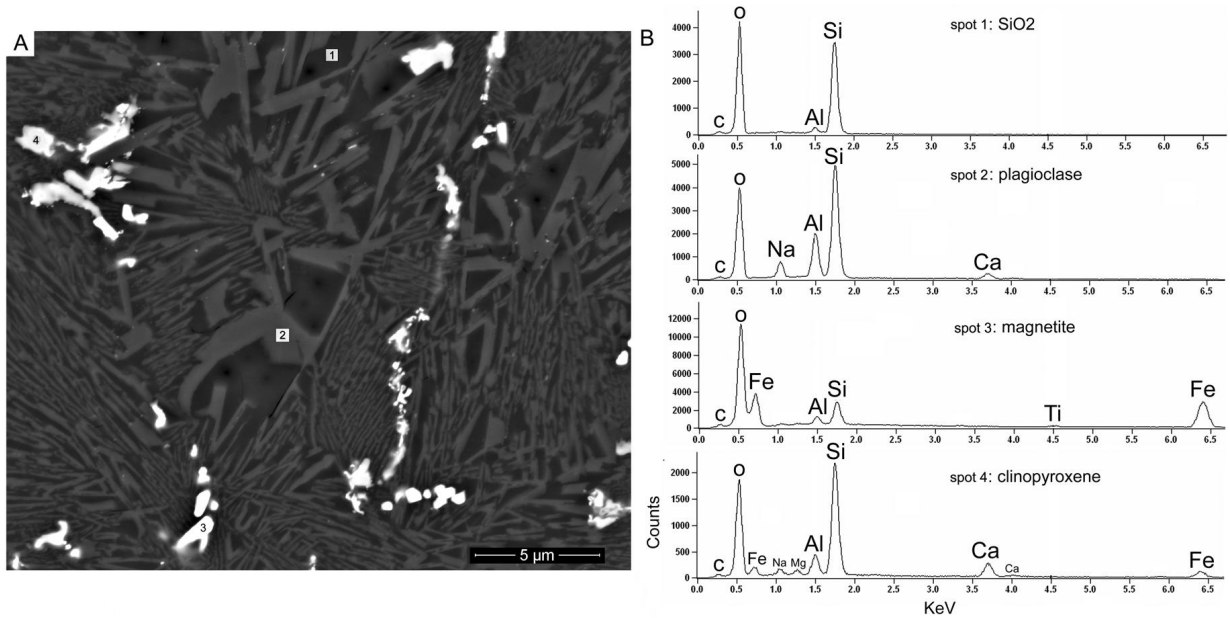

FIGURE 2. (**a**) BSE image of the internal texture of a spherulite showing energy dispersive spectroscopy (EDS) analysis points. (**b**) Representative EDS spectra of the mineral phases comprising the spherulite pictured in **a**. The small Al peak in the SiO_2 spectrum arises from contamination from an adjacent feldspar grain. Similarly, the Al and Si peaks in the magnetite are from the electron beam sampling small quantities of adjacent phases.

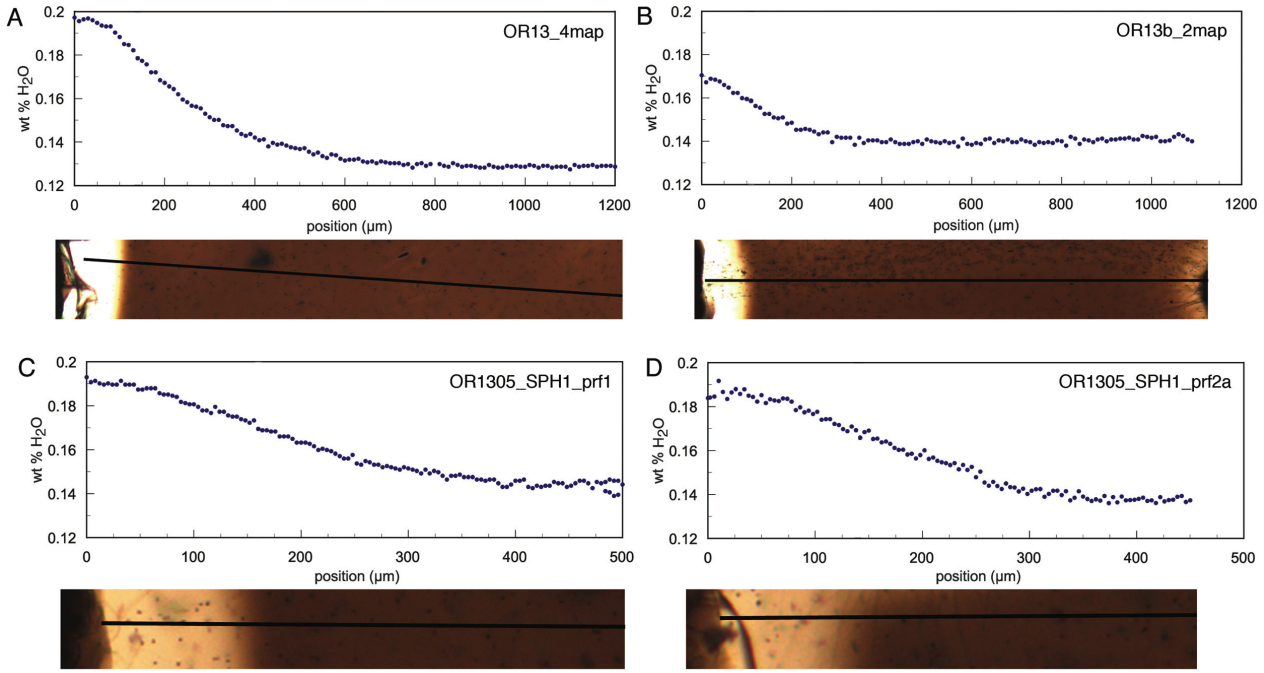

FIGURE 3. Water concentration profiles around spherulites in obsidian. The LHS of the diagrams corresponds to spherulite-glass margin, as seen in the subjacent photomicrographs of the corresponding samples.

TABLE 2. Properties of water concentration profiles around spherulites

Spherulite	*R* (µm)*	Prof†	Length (µm)‡	OH-min§	OH-max‖	OH-actual (mg)#	OH-predicted (mg)**
OR1305_A	730	1map	900	0.131	0.195	0.36	0.5
	730	4map	900	0.13	0.197	0.37	0.5
OR1305_SPH1	460	prf1	450	0.134	0.186	0.129	0.129
	460	prf2a	450	0.137	0.188	0.121	0.129
OR1305_D	318	T1map	360	0.132	0.165	0.032	0.042
	318	T2map	380	0.125	0.161	0.041	0.042
OR1305_B	286	2map	370	0.135	0.164	0.029	0.031
	286	3map	350	0.131	0.156	0.028	0.031
OR1305_2	260	2bmap	350	0.131	0.155	0.02	0.023

* Spherulite radius.
† Profile label.
‡ Profile length.
§ Minimum OH^- concentration along profile in wt%.
‖ Maximum OH^- concentration along profile in wt%.
Amount of water rejected during spherulite growth, measured.
** Amount of water rejected during spherulite growth, predicted.

SPHERULITE CRYSTALLIZATION KINETICS

It is clear from the mass-volume balance between the OH^- concentrations and the corresponding volume of the spherulites that the concentration profiles were produced by the rejection of water during the growth of anhydrous minerals in the spherulites. As the spherulites grew and expelled water outwardly, the flux of water at the spherulite edge was counter balanced by diffusion of water away from the spherulite-melt/glass boundary. Thus, spherulite growth (i.e., advection) and diffusion worked in concert to produce the natural water concentration profiles.

By modeling the combined growth and diffusion processes, and comparing model and natural water concentration profiles, we can estimate timescales of spherulite growth. Specifically, we solved numerically the advection-diffusion equation in spherically symmetrical form within the reference frame of the moving spherulite-melt/glass boundary (Crank 1984):

$$\frac{\partial C}{\partial t} + u \cdot \frac{\partial C}{\partial r} = D(C,T,P)\left(\frac{\partial^2 C}{\partial r^2} + \frac{2}{r} \cdot \frac{\partial C}{\partial r}\right), \quad (r > r_i). \qquad (1)$$

Here, t is time, r is the spherulite radius, r_i is the crystal/melt interface position, C is the concentration of OH^- species, and D is the diffusivity of H_2O in the melt. We note that even though OH^- is the dominant hydrous species measured in these obsidians, diffusion of hydrous species likely occurs through the migration of molecular H_2O (e.g., Zhang et al. 1991). Consequently, our model calculates the diffusivity of molecular H_2O, which changes with T, P, and C according to the formula of Zhang and Behrens (2000).

The second term on the LHS of Equation 1 represents advection, and requires the choice of a spherulite growth law that will dictate the velocity of the spherulite-matrix interface, u or dr_i/dt. This velocity, in turn, determines the flux of water extruded from the moving boundary after each time step.

The form of the spherulite growth law is an a priori unknown function of time. We assume that the growth rate decreased exponentially with time; this assumption is justified for the case that growth was limited by the diffusion rates of crystal nutrients

toward the growth boundary, and possibly by diffusion of hydrous species and other impurities away from the boundary (e.g., Frank 1950; Keith and Padden 1964; Granasy et al. 2005). We chose the following exponential growth law:

$$\frac{dr_i}{dt} = R\frac{2}{\sqrt{\pi}}\exp\left[-\left(\frac{t}{\tau}\right)^2\right] \quad (2)$$

where the parameter τ is the spherulite growth timescale and the primary fitting parameter, and R is the spherulite radius.

The numerical model calculates by finite difference the amount of water released at the spherulite-matrix boundary per each increment of growth; the amount of water ejected is determined by mass conservation at the boundary:

$$\left(\int_0^L 4\pi r^2 C(r)dr\right)_{t=0} = \left(\int_{r_i}^L 4\pi r^2 C(r)dr\right)_t \quad (3)$$

where L is the width of the matrix. The initial water concentration prior to spherulite growth is the average OH^- value measured in the "far field" along the flat part of the profile. In the model, mass transport takes place solely in the radial direction away from the interface (Fig. 4).

The modeling routine involves varying the growth timescale (τ), which is the amount of time that the model runs to reach the target spherulite radius, iteratively to produce the best fit to the natural data. Other model input parameters include the measured spherulite size, a fixed temperature, and P = 0.1 MPa. As the temperature is not well constrained, we have modeled a range of bracketing temperatures (see discussion below). The model does not account for the latent heat of crystallization.

We assume that the natural water profiles developed largely during spherulite growth. However, there is evidence that water continued to diffuse after the interface had stopped moving, namely in the form of the profile inflection points, manifested as downturns in the concentration near the spherulite-glass border. These points may arise because the flux of water from the spherulite shuts off when growth ceases, yet diffusion of water due to the concentration gradient at the spherulite margin may continue.

Our model accounts for post-growth diffusion by calculating the concentration profile under a no-flux boundary condition after the spherulite grows to its final size. The amount of post-growth diffusion is not known a priori. However, because we are interested in determining maximum spherulite growth timescales, we ran models with the smallest amount of post-growth diffusion that would properly fit the profiles. We found that a minimum of 6% (i.e., 6% of the growth timescale) post-growth diffusion was required to best fit the natural data. Model simulations with <6% post-growth diffusion did not produce a large enough downturn in the concentration profile, while simulations incorporating more post-growth diffusion required shorter spherulite growth timescales (i.e., less syn-growth diffusion).

Figure 4b shows an example of a calculation with and without post-growth diffusion; the model with post-growth diffusion reproduces the downturn near the spherulite-glass border and the inflection point on the profile well. The crystallization temperature is an unknown. The observation that spherulites deflect the banding in some samples (Fig. 1c) indicates that crystallization may have begun above the glass transition temperature (T_g), where the melt was capable of viscous deformation. In most samples however, spherulites overprint banding; thus their growth must have continued after that viscous deformation had ceased. Evidence that spherulite growth continued below T_g includes the birefringent haloes (Fig. 1b). Birefringence reflects anisotropy

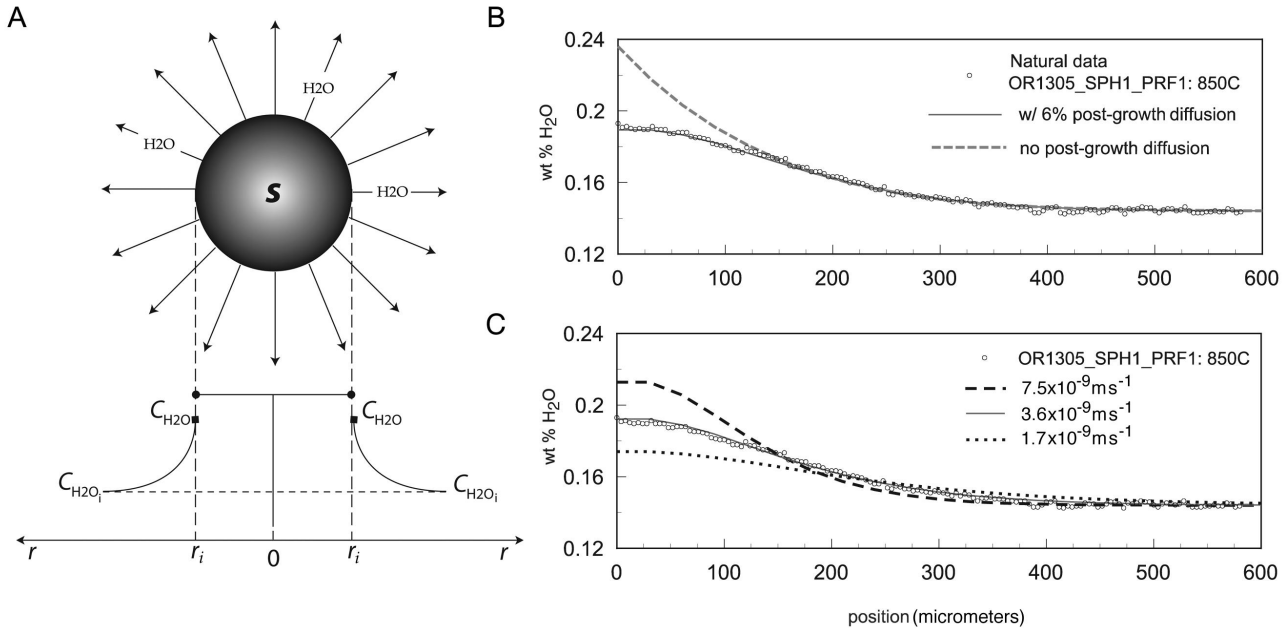

FIGURE 4. (**a**) Schematic of a spherulite (S) growing and extruding water (H_2O). Vertical dashed lines demarcate the spherulite boundary ($r = r_i$) at a given time ($t > 0$); the horizontal dashed line indicates the initial water concentration ($C_{H_2O}i$). (**b**) Comparison of natural concentration data (circles) and diffusion simulations with (solid line) and without (dashed) a 6% post-growth diffusion. (**c**) Model fits to natural data. Shown are a best fit (solid curve) and models run at bracketing growth rates.

in the glass, which results from unrelaxed stress accumulation during hydration as the spherulites grew (e.g., Friedman and Smith 1960). The preservation of anisotropy, therefore, shows that some of the growth took place below T_g, otherwise, the expansion of the melt structure due to hydration would have been accommodated by flowage of the melt around the hydrous region and subsequent strain relaxation in the hydrous zone.

Differential scanning calorimetric measurements constrain T_g of these obsidians to be about 690 °C (±20 °C). Because our diffusion model only operates at a fixed temperature, we modeled spherulite growth near the glass transition, at 700 °C, in addition to bracketing temperatures of 650, 800, and 850 °C. The resultant diffusion curves were superimposed on the natural data (Fig. 4c). The best-fit growth timescales were then converted to average linear growth rates by dividing the growth timescale by the observed spherulite size (Table 3). Average linear growth rates are minimum values, and are used solely to compare model results at different temperatures and to examine possible variations in growth rate with spherulite size.

Spherulite growth timescales range from about 1 day to nearly 2 weeks depending on the temperature (Fig. 5a; Table 3). The growth timescale of the largest spherulite (OR1305_A) is discordant, probably because this spherulite had retained water during its growth (Table 3). In this case, the profile (Fig. 3a) appears to be more evolved than it actually is, and a longer diffusion time was required to properly fit the profile (complete profile data are available in an electronic supplement[1]).

Spherulite growth timescales are remarkably consistent at each model temperature (Table 3). This finding makes geological sense, in that the spherulites come from a relatively small region of melt, one that would have experienced roughly the same cooling rate. Gottsmann and Dingwell (2001) determined the cooling rates of compositionally similar spherulitic obsidians to be about ~0.003–0.0006 °C/s, implying timescales of about 20–100 h to cool from 850–650 °C. This cooling interval falls within the range of spherulite growth timescales determined from the concentration profiles, and thus, provides an independent check on our results.

Spherulite growth rates calculated from growth timescales vary by about one order of magnitude (~10^{-10}–10^{-9} m/s) across

[1] Deposit item AM-08-057, electronic supplement. Deposit items are available two ways: For a paper copy contact the Business Office of the Mineralogical Society of America (see inside front cover of recent issue) for price information. For an electronic copy visit the MSA web site at http://www.minsocam.org, go to the American Mineralogist Contents, find the table of contents for the specific volume/issue wanted, and then click on the deposit link there.

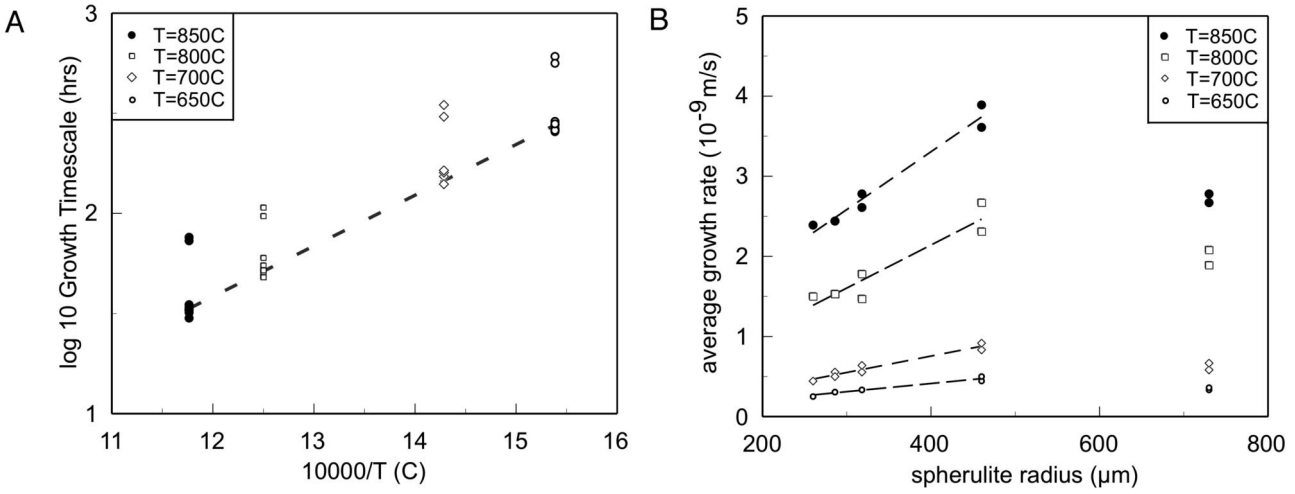

FIGURE 5. (**a**) Logarithm of the best-fit growth timescale vs. reciprocal temperature. Linear data arrays reflect Arrhenian dependence of D_{H_2O} on temperature. The upper data array represents calculations for two profiles measured on the largest spherulite (OR1305_A; r = 730 µm); this spherulite had retained water and thus the results demonstrate the error associated with incomplete extrusion of water during growth. The lower data comprise measurements on four smaller spherulites. (**b**) Average linear growth rate vs. spherulite size. The slopes of the linear fits are equal to the inverse growth timescale.

TABLE 3. Growth timescales (*t* in h)* and rates (G in m/s) determined from diffusion model fits to water concentration profiles

Profile	850 °C		800 °C		700 °C		650 °C	
	t	G	*t*	G	*t*	G	*t*	G
1map	76 (4.6)	2.67E-9	107 (6.4)	1.89E-9	348 (20.9)	5.83E-10	608 (36.5)	3.33E-10
4map	73 (4.4)	2.78E-9	97 (5.8)	2.08E-9	304 (18.2)	6.67E-10	562 (33.7)	3.61E-10
prf1	35 (2.1)	3.61E-9	55 (3.3)	2.31E-9	153 (9.2)	8.33E-10	288 (17.3)	4.44E-10
prf2a	33 (2.0)	3.89E-9	48 (2.9)	2.67E-9	140 (8.4)	9.17E-10	256 (15.4)	5.00E-10
T1map	34 (2.0)	2.61E-9	60 (3.6)	1.47E-9	160 (9.6)	5.56E-10	276 (16.6)	3.33E-10
T2map	32 (1.9)	2.78E-9	50 (3.0)	1.78E-9	140 (8.4)	6.39E-10	265 (15.9)	3.33E-10
2map	33 (2.0)	2.44E-9	52 (3.1)	1.53E-9	140 (8.4)	5.56E-10	260 (15.6)	3.06E-10
3map	33 (2.0)	2.44E-9	52 (3.1)	1.53E-9	160 (9.6)	5.00E-10	260 (15.6)	3.06E-10
2bmap	30 (1.8)	2.39E-9	48 (2.9)	1.50E-9	164 (9.8)	4.44E-10	280 (16.8)	2.50E-10

* Values in parentheses represent the amount of post-growth diffusion (in h) imposed in the model simulations.

the 200 °C range of temperature (Fig. 5b). These data define a range of permissible growth rates in the event that cooling was important during spherulite growth. For example, if a spherulite began to grow at 800 °C and stopped growing at 700 °C, then the effective average growth rate would be intermediate to the bounding isothermal-model-derived values, as cooling would cause the growth rate to slow down from the value at 800 °C.

The average growth rates closely match the values determined experimentally in model orthoclase-quartz eutectic melts ($\sim 10^{-10}$–10^{-9} m/s; Baker and Freda 2001). By contrast, the growth rates determined herein exceed the values determined experimentally in synthetic water-saturated rhyolite melts ($\sim 10^{-13}$–10^{-11} m/s; Swanson 1977). Interpreting our results in the context of experimental studies is not warranted beyond these simple comparisons due to the fact that several variables in the natural system, such as temperature, are not precisely known.

With the exception of the largest spherulite (OR1305_A), the average growth rates increase linearly with spherulite size at a given temperature, reflecting size-dependent growth (Fig. 5). Size-dependent crystal growth has been observed in crystallization experiments (Randolf and Larson 1988). In such experiments, larger crystals typically grow faster than smaller ones. It has also been observed that equal-sized crystals in close proximity to one another may grow at disparate rates. Apart from the data presented in this paper, these phenomena have not been documented in natural systems; however, size-dependent and dispersive growth have been proposed as mechanisms to generate lognormal crystal-size distributions common in igneous rocks (e.g., Eberl et al. 2002). That individual spherulites may grow at different rates has important implications for interpreting CSDs in natural volcanic rocks, which have typically assumed constant-rate crystal growth (e.g., Cashman 1988). Thorough testing of CSD models awaits collection of a larger data set of spherulite growth rates.

Concluding remarks

Water concentration profiles around spherulites are quite literally the frozen-in signatures of chemical diffusion driven by phase transformation in silicate melt at high temperature. SFTIR measurements of natural water profiles confirm the genetic relationship between the spherulite growth and volatile enrichment in glassy rhyolite. The shapes of diffusion patterns around spherulites are consistent with combined advective and diffusive transport of water during spherulite growth, followed by a small amount of post-growth diffusion. Diffusion modeling yields spherulite growth rates of a few tenths to hundredths of a millimeter per day, depending on temperature. Diffusion models also suggest that spherulites may grow according to a size-dependent growth mechanism.

Acknowledgments

This research was supported by the Alexander von Humboldt Foundation. The comments of Yan Liang, Samuel E. Swanson, and Don Baker are wholeheartedly appreciated.

References cited

Baker, D.R. and Freda, C. (2001) Eutectic crystallization in the undercooled Orthoclase-Quartz-H_2O system: experiments and simulations. European Journal of Mineralogy, 13, 453–466.

Cashman, K.V. (1988) Crystallization of Mount St. Helens dacite; a quantitative textural approach. Bulletin of Volcanology, 50, 194–209.

Castro, J.M., Manga, M., and Martin, M.C. (2005) Vesiculation rates of obsidian domes inferred from H_2O concentration profiles. Geophysical Research Letters, 32, L21307, DOI: 10.1029/2005GL024029.

Costa, F. and Dungan, M. (2005) Short time scales of magmatic assimilation from diffusion modeling of multiple elements in olivine. Geology, 33, 837–840.

Crank, J. (1984) Free and Moving Boundary Problems, 436 p. Clarendon Press, Oxford, U.K.

Eberl, D.D., Kile, D.E., and Drits, V.A. (2002) On geological interpretations of crystal size distributions: Constant vs. proportionate growth. American Mineralogist, 87, 1235–1241.

Frank, F.C. (1950) Radially symmetric phase growth controlled by diffusion. Proceedings of the Royal Society of London, Series A, 201, 586–599.

Friedman, I. and Smith, R.L. (1960) A new dating method using obsidian: Part I, The development of the method. American Antiquity, 25, 476–493.

Gaillard, F., Schmidt, B., Mackwell, S., and McCammon, C. (2003) Rate of hydrogen-iron redox exchange in silicate melts and glasses. Geochimica et Cosmochimica Acta, 67, 2427–2441.

Ghiorso, M.S. and Sack, R.O. (1995) Chemical mass transfer in magmatic processes IV: A revised and internally consistent thermodynamic model for the interpolation and extrapolation of liquid-solid equilibria in magmatic systems at elevated temperatures and pressures. Contributions to Mineralogy and Petrology, 119, 197–212.

Gonnermann, H. and Manga, M. (2007) The fluid mechanics inside a volcano. Annual Reviews of Fluid Mechanics, 39, 321–356.

Gottsmann, J. and Dingwell, D.B. (2001) The cooling of frontal flow ramps: a calorimetric study on the Rocche Rosse rhyolite flow, Lipari, Aeolian Islands, Italy. Terra Nova, 13, 157–164.

Gottsmann, J., Giordano, D., and Dingwell, D.B. (2002) Predicting shear viscosity during volcanic processes at the glass transition: A calorimetric calibration. Earth and Planetary Science Letters, 198, 417–427.

Granasy, L., Pusztai, T., Gyorgy, T., Warren, J., and Douglas, J. (2005) Growth and form of spherulites. Physical Review E, 72, 011605.

Keith, H.D. and Padden Jr., F.J. (1964) Spherulitic crystallization from a melt. II. Influence of fractionation and impurity segregation on the kinetics of crystallization. Journal of Applied Physics, 35, 1286–1296.

MacLellan, H.E. and Trembath, L.T. (1991) The role of quartz crystallization in the development and preservation of igneous texture in granitic rocks: Experimental evidence at 1 kbar. American Mineralogist, 76, 1291–1305.

Manley, C.R. (1992) Extended cooling and viscous flow of large, hot rhyolite lavas: Implications of numerical modeling results. Journal of Volcanology and Geothermal Research, 53, 27–46.

Manley, C.R. and Fink, J.H. (1987) Internal textures of rhyolite flows as revealed by research drilling. Geology, 15, 549–552.

Newman, S., Stolper, E.M., and Epstein, S. (1986) Measurement of water in rhyolitic glasses: Calibration of an infrared spectroscopic technique. American Mineralogist, 71, 1527–1541.

Randolf, A.D. and Larson, M.A. (1988) Theory of particulate processes, second edition, 369 p. Academic Press, New York.

Smith, R.K., Tremallo, R.L., and Lofgren, G.E. (2001) Growth of megaspherulites in a rhyolitic vitrophyre. American Mineralogist, 86, 589–600.

Sparks, R.S.J. (1997) Causes and consequences of pressurization in lava dome eruptions. Earth and Planetary Science Letters, 150, 177–189.

Stasiuk, M.V., Barclay, J., Carroll, M.R., Jaupart, C., Ratte, J.C., Sparks, R.S.J., and Tait, S.R. (1996) Degassing during magma ascent in the Mule Creek vent (U.S.A.). Bulletin of Volcanology, 58, 117–130.

Stevenson, R.J., Hodder, A.P.W., and Briggs, R.M. (1994) Rheological estimates of rhyolite lava flows from the Okataina volcanic centre, New Zealand. New Zealand Journal of Geology and Geophysics, 37, 211–221.

Swanson, S.E. (1977) Relation of nucleation and crystal-growth rate to the development of granitic textures. American Mineralogist, 62, 966–978.

Swanson, S.E., Naney, M.T., Westrich, H.R., and Eichelberger, J.C. (1989) Crystallization history of Obsidian Dome, Inyo Domes, California. Bulletin of Volcanology, 51, 161–176.

Westrich, H.R., Stockman, H.W., and Eichelberger, J.C. (1988) Degassing of rhyolitic magma during ascent and emplacement. Journal of Geophysical Research, 93, 6503–6511.

Wright, F.E. (1915) Obsidian from Hrafntinnuhryggur, Iceland: Its lithophysae and surface markings. Bulletin of the Geological Society of America, 26, 255–286.

Zhang, Y., Stolper, E.M., and Wasserburg, G.J. (1991) Diffusion of water in rhyolitic glasses. Geochimica et Cosmochimica Acta, 55, 441–456.

Zhang, Y. and Behrens, H. (2000) H_2O diffusion in rhyolitic melts and glasses. Chemical Geology, 169, 243–262.

Manuscript received December 23, 2007
Manuscript accepted July 1, 2008
Manuscript handled by Don Baker